

Structure and particle transport in second-order Stokes flow

Russell G. Keanini*

Department of Mechanical Engineering and Engineering Science, University of North Carolina at Charlotte, Charlotte, North Carolina 28223

(Received 8 February 1999; revised manuscript received 13 December 1999)

Second-order streaming in a thin fluid layer driven by one or two opposed, tangentially oscillating wavy walls is theoretically investigated. In contrast to the well-studied problem of oscillatory flow past a stationary boundary, the present problem is subject to a nonhomogeneous second-order boundary velocity condition. A combination of steady Reynolds stresses and boundary forcing thus drives the streaming flow; indeed, under most conditions, boundary-forced flow dominates Reynolds-stress-driven flow. The first part of the paper examines parametric effects on second-order flow structure. Under low-Reynolds-stress conditions and during single-boundary forcing, flow structure remains essentially independent of all parameters, including the Stokes layer thickness, the fluid layer thickness, and the forcing wave form. Three approximations to the full second-order solution, valid under low-Reynolds-stress conditions, are used to explain these results. In the case of dual-boundary forcing, no corresponding universal behaviors are observed; flow structure exhibits sensitivity to all problem parameters. The second part of the paper investigates particle transport during quasistatic second-order streaming. Here, slow, superposed, large-amplitude oscillations of one wall produce the time-dependent, quasisteady flows of interest. Collective particle motion in the direction of large-scale boundary displacement and filamentary motion in the opposite direction, features consistent with transport in traveling waves [E. Moses and V. Steinberg, *Phys. Rev. Lett.* **60**, 2030 (1988)], characterize short-time transport. Long-time or asymptotic transport, in contrast, is characterized by particle attraction or repulsion to or from period-one elliptic points and attraction toward limit cycles on the Poincaré map.

PACS number(s): 47.15.Gf, 47.90.+a

I. INTRODUCTION

Second-order streaming produced by oscillating solid boundaries, oscillatory flow over solid boundaries, or free surface wave motion plays an important role in wave-induced mass transport [1,2], formation of marine bottom topographies [3,4,5], heat transfer [6,7], acoustic levitation (see, e.g., [8]), and mass transfer [9], and presumably plays a significant role in acoustic particle agglomeration (see, e.g., [10]). Steady Reynolds stresses have traditionally been identified as the primary mechanism driving such flows. This picture holds that Reynolds stresses within near-boundary or interfacial Stokes layers induce cellular flow within the Stokes layer. Due to a nonzero slip velocity at the Stokes layer's outer edge, an outer flow is produced whose character is determined by the streaming Reynolds number $Re_s = \hat{U}_\infty^2 / \hat{\omega} \hat{\nu}$, where \hat{U}_∞ is a characteristic speed, $\hat{\omega}$ is the oscillation frequency, and $\hat{\nu}$ is the kinematic viscosity. For $Re_s \gg 1$, the outer flow assumes a boundary layer structure, while for $Re_s \ll 1$, the outer flow exists as an extended Stokes flow (see, e.g., [11,12]). In the present problem, where we limit attention to $Re_s \ll 1$, secondary flow is determined by *two* physical mechanisms: Reynolds stresses within the Stokes layer, and boundary forcing due to the no-slip boundary condition at the oscillating boundary.

Earlier theories of second-order streaming near wavy walls have focused exclusively on the case where a single wavy boundary remains fixed relative to a semi-infinite, os-

cillatory flow [3–5]. Lyne [3] considered second-order streaming in the limits where oscillation amplitudes (\hat{A}) are much smaller and much larger than the wall wavelength ($\hat{\lambda}$), $\epsilon \ll 1$ and $\epsilon \gg 1$, respectively, where $\epsilon = \hat{A} / \hat{\lambda}$. Vittori [5] adapted Lyne's [3] analysis to the case where wall protrusions consist of small sinusoids superposed on a larger primary sine wave (where the latter was treated by Lyne). She also extended Lyne's model by obtaining solutions valid for arbitrary values of $\hat{A} / \hat{\lambda}$. Kaneko and Honji [4] also extended Lyne's analysis by considering higher-order corrections in $\hat{h}_0 / \hat{\delta}$, where \hat{h}_0 is the wall amplitude and $\hat{\delta} = \sqrt{\hat{\nu} / \hat{\omega}}$ is the Stokes layer thickness. In this case, theoretical predictions were qualitatively consistent with flow visualization data. Soon after, Kaneko [13] reported numerical solutions for the same problem. Earlier work by Schlichting [14], Longuet-Higgins [1], Stuart [11], and Riley [12] provided much of the conceptual framework for these later studies.

This paper develops a two-dimensional theory of steady streaming within a finite fluid layer, driven by one or two opposing oscillatory wavy boundaries. The asymptotic model is appropriate in the limit where the streaming Reynolds number $Re_s \ll 1$, and assumes that $1 \gg \epsilon \gg \epsilon_w$, where $\epsilon_w (= \hat{h}_0 / \hat{\lambda})$ is the nondimensional wall amplitude. The work is motivated by a desire to better understand scalar transport across fluid gaps bounded by either regular or random surfaces, which in turn are subject to either regular or random vibration. We limit attention to periodic forcing, and in the first half of the paper extend earlier work [3–5,13] by examining the effects of fluid layer thickness, Stokes layer thickness, forcing wave form, driving frequency ratio, and opposing wall offset on secondary flow structure. A key

*FAX: (704) 547-2352. Electronic address: rkeanini@uncc.edu

finding, applicable under low-Reynolds-stress conditions, concerns the insensitivity of single-boundary-driven flow to variations in the first three parameters. Three approximations to the full second-order solution, valid under low-Reynolds-stress conditions, are derived and used to explain these results.

In the second half of the paper, we initiate study of long-range mass transport induced by slow, superposed quasistatic oscillations of one wall. While this type of transport has been investigated in generic Stokes flows (see, e.g., [15]), it has not been examined in second-order Stokes flows. Here we identify a pair of flow bifurcations, characterized by cross-channel stagnation streamlines “jumping” two wall wavelengths along a boundary, and occurring when crests and valleys on opposing walls pass through vertical alignment, as the critical mechanism mediating long-range particle transport. We then show that short-time transport, occurring on the slow (quasistatic) oscillation time scale, is consistent with observed transport in traveling waves and that long-time (asymptotic) transport is dominated by agglomeration or repulsion to or from moving elliptic points, or by periodic, collective rotation, also about moving elliptic points. These observations are interpreted in nonlinear dynamical terms.

II. PROBLEM FORMULATION: SINGLE OSCILLATING BOUNDARY

Second-order streaming within fluid layers bounded by opposing wavy walls is characterized by a number of length scales. In the simplest case, which we treat here, both walls have the same wavelength and amplitude and are subject to tangential forcing of the same amplitude. In this instance, five length scales can be identified: the wall wavelength $\hat{\lambda}$, the wall amplitude \hat{h}_0 , the amplitude of oscillation \hat{A} , the characteristic Stokes layer thickness $\hat{\delta} = \sqrt{\hat{\nu}/\hat{\omega}}$, and the mean depth of the fluid layer \hat{H} . Based on these scales, four independent parameters $\epsilon = \hat{A}/\hat{\lambda}$, $\sqrt{\beta} = \hat{\lambda}/\hat{\delta}$, $\epsilon_w = \hat{h}_0/\hat{\lambda}$, and $H = \hat{H}/\hat{\lambda}$ arise, indicating in turn the relative magnitude of particle displacements, the relative penetration of unsteady vorticity into the surrounding fluid, the relative height of wall protrusions, and the relative width (aspect ratio) of the fluid layer. By comparison, second-order streaming within semi-infinite fluid domains bounded by a single wavy wall is characterized by four length scales and three independent parameters [3–5], while steady streaming about compact cylinders and spheres in infinite domains is described by three length scales and two independent parameters [11,12].

We initially develop the solution for steady second-order flow produced by a single oscillating boundary and then extend this result to the case where both boundaries oscillate. Thus, consider two-dimensional flow within a finite fluid layer driven by an oscillating wavy wall, as shown in Fig. 1. For simplicity, we assume that both walls have the same wavelength and wave amplitude, $\hat{\lambda}$ and \hat{h}_0 . It should be noted, however, that the formulation can be modified to handle the more general case where each wall has a unique wavelength and amplitude. All lengths are nondimensionalized using the wall wavelength, while time is nondimensionalized using $\hat{\omega}$:

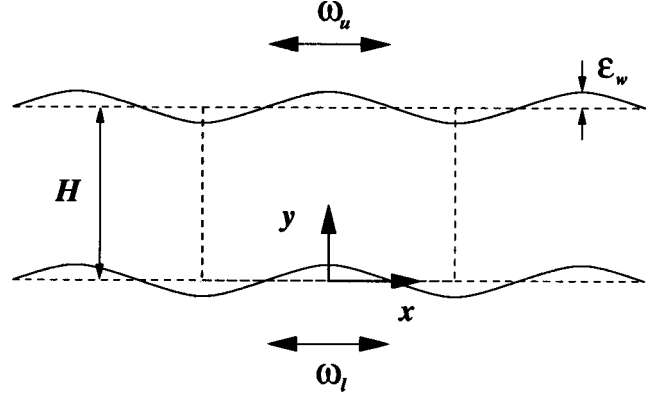


FIG. 1. The flow geometry.

$$(\mathbf{x}, H, \epsilon, \epsilon_w, \delta) = \hat{\lambda}^{-1}(\hat{\mathbf{x}}, \hat{H}, \hat{A}, \hat{h}_0, \hat{\delta}), \quad t = \hat{\omega} \hat{t}, \quad (1)$$

where $\hat{\mathbf{x}}$ is the position vector. In addition, velocity and the stream function are nondimensionalized using the wall velocity amplitude,

$$\mathbf{u} = (\hat{U}_\infty)^{-1} \hat{\mathbf{u}}, \quad \psi = (\hat{U}_\infty \hat{\lambda})^{-1} \hat{\psi}, \quad (2)$$

where $\hat{U}_\infty = \hat{A} \hat{\omega}$. Note that dimensional quantities are denoted with carets.

Taking the curl of the momentum equation and using the above definitions, we obtain the equation governing vorticity transport:

$$\partial_t \nabla^2 \psi - \epsilon \frac{\partial(\psi, \nabla^2 \psi)}{\partial(x, y)} = \beta^{-1} \nabla^4 \psi. \quad (3)$$

As a point of comparison with earlier work, β is roughly equivalent to the parameter $M^2 = \epsilon^{-2} \text{Re}_s$ introduced by Riley [12] while $\sqrt{\beta}$ is inversely proportional to the parameter k used by Lyne [3] ($\sqrt{\beta} = \sqrt{8} \pi/k$). Similarly, ϵ corresponds to the parameter kR introduced by Lyne.

The time- and space-dependent height h of the oscillating boundary, obtained via a Galilean transformation between wall-fixed and laboratory fixed coordinates, is given by

$$y = h(x, t) = \epsilon_w \cos\{k[x - \epsilon F(t)]\}, \quad (4)$$

where $k = 2\pi$ is the dimensionless wave number for the wall and $F(t)$ is the time-dependent tangential boundary displacement. In the following, we express $F(t)$ as

$$F(t) = \sum_{n=1}^{\infty} \frac{a_n}{n} \sin nt. \quad (5)$$

The velocity of the lower boundary, $\mathbf{u}_B = F'(t) \hat{\mathbf{i}}$, is purely horizontal and leads to the following conditions on ψ :

$$\partial_y \psi = F', \quad \partial_x \psi = 0, \quad y = h(x, t). \quad (6)$$

Similar conditions, with $F'(t)$ replaced by zero and y by $H - y$, are imposed on the upper surface.

We assume that $1 \gg \epsilon \gg \epsilon_w$ and expand ψ in ϵ and ϵ_w as follows:

$$\psi = \psi_{00} + \epsilon \psi_{10} + \epsilon_w \psi_{01} + \epsilon^2 \psi_{20} + \epsilon \epsilon_w \psi_{11} + \dots \quad (7)$$

This expansion differs from those used in [3,5], where the stream function was expanded in ϵ_w and steady streaming was obtained as an $O(\epsilon)$ correction to the $O(\epsilon_w)$ solution. Thus, the earlier solutions apply when $1 \gg \epsilon_w \gg \epsilon$. Transferring the boundary conditions in Eq. (6) to $y=0$ and similar conditions on the upper boundary to $y=H$, we obtain the following hierarchy of problems at $O(\epsilon^l \epsilon_w^j)$:

$$\partial_t \nabla^2 \psi_{IJ} + S_{IJ} = \frac{1}{\beta} \nabla^4 \psi_{IJ}, \quad (8)$$

$$\partial_y \psi_{IJ} = F_{IJ}(t), \quad y=0, \quad (9)$$

$$\partial_x \psi_{IJ} = 0, \quad y=0, \quad (10)$$

$$\partial_y \psi_{IJ} = 0, \quad y=H, \quad (11)$$

$$\partial_x \psi_{IJ} = 0, \quad y=H. \quad (12)$$

Here, S_{IJ} is a vorticity source term at $O(\epsilon^l \epsilon_w^j)$ and F_{IJ} is a corresponding horizontal boundary velocity. It is readily shown that $S_{00} = S_{01} = S_{10} = S_{20} = 0$. At $O(\epsilon \epsilon_w)$, however, the source term assumes the form

$$S_{11} = -\mathbf{k} \cdot \nabla \times (\mathbf{u}_{00} \cdot \nabla \mathbf{u}_{01} + \mathbf{u}_{01} \cdot \nabla \mathbf{u}_{00}), \quad (13)$$

where for convenience S_{11} is expressed in terms of the $O(1)$ and $O(\epsilon_w)$ velocity fields, \mathbf{u}_{00} and \mathbf{u}_{01} , respectively. The boundary velocities at each order are given by

$$F_{00} = F'(t) = \sum_{n=1}^{\infty} a_n \cos nt, \quad (14)$$

$$F_{10} = 0, \quad (15)$$

$$F_{01} = -\cos(kx) \partial_{yy} \psi_{00}, \quad (16)$$

$$F_{20} = 0, \quad (17)$$

$$F_{11} = -kF(t) \sin(kx) \partial_{yy} \psi_{00}. \quad (18)$$

As seen above, the $O(\epsilon)$ and $O(\epsilon^2)$ problems are homogeneous so that $\psi_{10} = \text{const}$ and $\psi_{20} = \text{const}$. Note too that transferring boundary conditions to the plane surfaces $y=0$ and $y=H$ allows a simpler formulation than the conformal transformation approach used by Lyne [3]. Transferring boundary conditions in, e.g., Eq. (6) from $y=h(x,t) = \epsilon_w \cos\{k[x - \epsilon F(t)]\}$ to $y=0$ is carried out by Taylor expanding derivatives of ψ about $y=0$ and by expanding the function $h(x,t)$ for small ϵ . Thus, for example, $\partial_y \psi(x,h,t) = \partial_y \psi(x,0,t) + \partial_{yy} \psi(x,0,t) [\epsilon_w \cos(kx) + \epsilon_w \epsilon k F \sin(kx)] + O(\epsilon^2 \epsilon_w)$. Inserting Eq. (7) into this expression then leads directly to the conditions in Eqs. (14)–(18).

A. $O(1)$ solution: generalized Stokes solution

The $O(1)$ solution to Eqs. (8)–(12) describes flow produced by a flat plate, driven by a cyclic tangential velocity $F'(t)$. To simplify derivation of higher-order solutions, we state the $O(1)$ solution in terms of the x velocity component (where the y component is zero):

$$u_{00} = \sum_{n=1}^{\infty} [A_n \exp(\nu_n \bar{y} + int) + B_n \exp(-\nu_n \bar{y} + int) + A_n^* \exp(\nu_n^* \bar{y} - int) + B_n^* \exp(-\nu_n^* \bar{y} - int)], \quad (19)$$

Here complex conjugates are starred, $\bar{y} = \sqrt{\beta} y$, $\bar{H} = \sqrt{\beta} H$, $\nu_n = \sqrt{n/2}(1+i)$, and

$$A_n = \frac{a_n/2}{1 - \exp(2\nu_n \bar{H})}, \quad B_n = -\frac{(a_n/2) \exp(2\nu_n \bar{H})}{1 - \exp(2\nu_n \bar{H})}.$$

It is readily shown that when $u_B = F'(t) = \cos(t)$ and $\bar{H} \rightarrow \infty$, this solution simplifies to Stokes' classical solution for flow in a semi-infinite region, driven by a flat, sinusoidally oscillating plate.

B. $O(\epsilon_w)$ solution

The $O(\epsilon_w)$ solution satisfying Eqs. (8)–(12) is given by

$$\psi_{01} = \cos(kx) \sum_{n=1}^{\infty} [\chi_n(\bar{y}) \exp(int) + \chi_n^*(\bar{y}) \exp(-int)], \quad (20)$$

where

$$\chi_n(\bar{y}) = A_1^{(n)} \exp(\omega_n \bar{y}) + A_2^{(n)} \exp(q \bar{y}) + A_3^{(n)} \exp(-\omega_n \bar{y}) + A_4^{(n)} \exp(-q \bar{y}), \quad (21)$$

and where the coefficients $A_1^{(n)}$, $A_2^{(n)}$, $A_3^{(n)}$, and $A_4^{(n)}$ are given in the Appendix.

Again, it can be shown that in the case where $F'(t) = \cos(t)$ and $\bar{H} \rightarrow \infty$, the solution in Eq. (20) simplifies to Lyne's [3] $O(\epsilon_w)$ solution.

C. $O(\epsilon \epsilon_w)$ solution: steady streaming due to arbitrary forcing

We first decompose ψ_{11} into steady and unsteady parts:

$$\psi_{11} = \psi_{11}^{(s)} + \psi_{11}^{(t)}, \quad (22)$$

where

$$\beta^{-1} \nabla^4 \psi_{11}^{(s)} = -\mathbf{k} \cdot \nabla \times (\mathbf{u}_{00} \cdot \nabla \mathbf{u}_{01} + \mathbf{u}_{01} \cdot \nabla \mathbf{u}_{00}) \Big|_{\text{steady}}, \quad (23)$$

$$\partial_y \psi_{11}^{(s)} = -\bar{g}_1(x) \partial_{yy} \psi_{00} \Big|_{\text{steady}}, \quad \partial_x \psi_{11}^{(s)} = 0, \quad y=0,$$

$$\partial_y \psi_{11}^{(s)} = 0, \quad \partial_x \psi_{11}^{(s)} = 0, \quad y=H,$$

and

$$\partial_t \nabla^2 \psi_{11}^{(t)} - \beta^{-1} \nabla^4 \psi_{11}^{(t)} = \mathbf{k} \cdot \nabla \times (\mathbf{u}_{00} \cdot \nabla \mathbf{u}_{01} + \mathbf{u}_{01} \cdot \nabla \mathbf{u}_{00}) \Big|_{\text{unsteady}}, \quad (24)$$

$$\partial_y \psi_{11}^{(t)} = -\bar{g}_1(x) \partial_{yy} \psi_{00} \Big|_{\text{unsteady}}, \quad \partial_x \psi_{11}^{(t)} = 0, \quad y=0,$$

$$\partial_y \psi_{11}^{(t)} = 0, \quad \partial_x \psi_{11}^{(t)} = 0, \quad y=H,$$

and where $\tilde{g}_1(x) = k \sin(kx)F(t)$.

Since we are interested only in the steady solution $\psi_{11}^{(s)}$, and since this problem is subject to two nonhomogeneities, we obtain the solution by superposing two subproblems, each subject to a single nonhomogeneous term:

$$\psi_{11}^{(s)} = \psi_{11}^{(1)} + \psi_{11}^{(2)}, \quad (25)$$

where

$$\beta^{-1} \nabla^4 \psi_{11}^{(1)} = -\mathbf{k} \cdot \nabla \times (\mathbf{u}_{00} \cdot \nabla \mathbf{u}_{01} + \mathbf{u}_{01} \cdot \nabla \mathbf{u}_{00})|_{\text{steady}},$$

$$\nabla^4 \psi_{11}^{(2)} = 0,$$

$$\begin{aligned} \partial_y \psi_{11}^{(1)} &= 0 \\ \partial_y \psi_{11}^{(2)} &= -\tilde{g}_1(x) \partial_{yy} \psi_{00}|_{\text{steady}}, \quad y=0, \end{aligned}$$

$$\partial_x \psi_{11}^{(1)} = \partial_x \psi_{11}^{(2)} = 0, \quad y=0,$$

$$\partial_y \psi_{11}^{(1)} = \partial_y \psi_{11}^{(2)} = 0, \quad y=H,$$

$$\partial_x \psi_{11}^{(1)} = \partial_x \psi_{11}^{(2)} = 0, \quad y=H.$$

Physically, $\psi_{11}^{(1)}$ is the second-order flow component produced by steady Reynolds stresses while $\psi_{11}^{(2)}$ is the component driven by the nonhomogeneous boundary velocity.

The final solution is given by

$$\begin{aligned} \psi_{11}^{(s)} &= \sin(kx) \sum_{n=1}^{\infty} \left\{ (a_1^{(n)} + b_1^{(n)}) e^{-q\tilde{y}} + (a_2^{(n)} + b_2^{(n)}) \tilde{y} e^{-q\tilde{y}} \right. \\ &\quad + (a_3^{(n)} + b_3^{(n)}) e^{q\tilde{y}} + (a_4^{(n)} + b_4^{(n)}) \tilde{y} e^{q\tilde{y}} \\ &\quad \left. + \sum_{j=1}^4 [C_j^{(n)} \exp(K_{jn}\tilde{y}) + D_j^{(n)} \exp(M_{jn}\tilde{y})] \right\} + \text{c.c.}, \end{aligned} \quad (26)$$

where the coefficients q , $a_1^{(n)} - a_4^{(n)}$, $b_1^{(n)} - b_4^{(n)}$, $C_j^{(n)}$, $D_j^{(n)}$, K_{jn} , and M_{jn} are given in the Appendix. It is important to note that the problem associated with an oscillating boundary is not equivalent to the problem associated with an oscillating fluid over a stationary boundary. The difference arises at $O(\epsilon\epsilon_w)$, where the nonhomogeneous boundary condition in Eq. (23) does not appear in the latter case.

III. STEADY STREAMING PRODUCED BY TWO OSCILLATING WAVY BOUNDARIES

We consider the simplest case where upper and lower boundaries are driven at single frequencies $\hat{\omega}^u$ and $\hat{\omega}^l$, respectively, and require that $\hat{\omega}^l/\hat{\omega}^u = P$ where $P = 2, 3, 4, \dots$. This condition allows us to construct a steady second-order solution by superposing the steady solution for single-frequency forcing at a single boundary. In particular, at any instant and over period $\hat{T} = 2\pi/\hat{\omega}_m$ [where $\hat{\omega}_m = \min(\hat{\omega}^u, \hat{\omega}^l)$] the cross-terms $\mathbf{u}_{00}^u \cdot \nabla \mathbf{u}_{01}^l$, $\mathbf{u}_{00}^l \cdot \nabla \mathbf{u}_{01}^u$, $\mathbf{u}_{01}^u \cdot \nabla \mathbf{u}_{00}^l$, and $\mathbf{u}_{01}^l \cdot \nabla \mathbf{u}_{00}^u$ in S_{11} and the terms $F^u(t) \psi'_{00,yy}$ and $F^l(t) \psi'_{00,yy}$ in the tangential velocity boundary conditions have zero steady components. Thus, superposing a modified version of $\psi_{11}^{(s)}$ in Eq. (26), which we denote as $\psi_{11}^{(su)}$ (and which corresponds

to flow produced by the upper boundary), with $\psi_{11}^{(s)}$, we obtain the overall solution:

$$\psi_{11}^{(s)} = \psi_{11}^{(sl)} + \psi_{11}^{(su)}, \quad (27)$$

where $\psi_{11}^{(sl)} = \psi_{11}^{(s)}$ [from Eq. (26)]. Letting $\gamma = \hat{\omega}^u/\hat{\omega}^l$ and noting that the index $n=1$, $\psi_{11}^{(su)}$ is obtained from the solution in Eq. (26) by introducing the following substitutions into the coefficients $a_1^{(1)} - a_4^{(1)}$, $b_1^{(1)} - b_4^{(1)}$, $C_j^{(1)}$, $D_j^{(1)}$, K_{j1} , and M_{j1} in Eq. (26): (i) replace ν_1 with $\sqrt{\gamma}\nu_1$; (ii) replace a_1 with γa_1 ; (iii) replace β with $\gamma\beta$; (iv) replace ω_1 with $\sqrt{q^2/\gamma + i\gamma}$; (v) replace q with $q/\sqrt{\gamma}$; (vi) premultiply any term containing n by γ [excepting those already mentioned in (i)–(v)]; (vii) replace \tilde{y} with $\tilde{H} - \tilde{y}$; and (viii) replace x with $1 - x$. Note that $\nu_1 = \sqrt{\frac{1}{2}(1+i)}$ and that the magnitudes of β and $q = 2\pi/\sqrt{\beta}$ are determined by $\hat{\omega}^l$, the frequency of the lower boundary. Also note that when crests and valleys on upper and lower walls are not vertically aligned x is replaced by

$$x' = 1 + \phi - x, \quad (28)$$

where ϕ is the horizontal distance between any given crest on the lower wall and the nearest crest lying to the right on the upper wall. We will refer to ϕ as the *wall offset*.

IV. APPROXIMATE SECOND-ORDER SOLUTIONS

This section briefly describes three approximations to the full second-order solution $\psi_{11}^{(s)}$ in Eq. (26), valid in the limit where Reynolds-stress-driven flow is negligible. Using superposition and the substitutions given in the last section, all three approximations are adapted to handle dual-boundary forcing (see below). The approximate ranges of validity are noted in each case.

A. Zero-Reynolds-stress approximation

As noted, the second-order solution in Eq. (26) represents the superposition of two flow components $\psi_{11}^{(1)}$ and $\psi_{11}^{(2)}$, where $\psi_{11}^{(1)}$, given by

$$\begin{aligned} \psi_{11}^{(1)} &= \sin(kx) \sum_{n=1}^{\infty} \left\{ a_1^{(n)} e^{-q\tilde{y}} + a_2^{(n)} \tilde{y} e^{-q\tilde{y}} + a_3^{(n)} e^{q\tilde{y}} \right. \\ &\quad + a_4^{(n)} \tilde{y} e^{q\tilde{y}} + \sum_{j=1}^4 [C_j^{(n)} \exp(K_{jn}\tilde{y}) \\ &\quad \left. + D_j^{(n)} \exp(M_{jn}\tilde{y})] \right\} + \text{c.c.}, \end{aligned} \quad (29)$$

is the component produced by steady Reynolds stresses and $\psi_{11}^{(2)}$, given by

$$\begin{aligned} \psi_{11}^{(2)} &= \sin(kx) \sum_{n=1}^{\infty} (b_1^{(n)} e^{-q\tilde{y}} + b_2^{(n)} \tilde{y} e^{-q\tilde{y}} + b_3^{(n)} e^{q\tilde{y}} \\ &\quad + b_4^{(n)} \tilde{y} e^{q\tilde{y}}) + \text{c.c.}, \end{aligned} \quad (30)$$

is the component produced by the nonzero second-order velocity on the oscillating boundary. It is found that over $10^{-2} \leq \beta \leq 10^3$ and $H \geq 0.2$, $\psi_{11}^{(s)}$ is well approximated by the second component alone, i.e.,

$$\psi_{11}^{(s)} \approx \psi_{11}^{(2)} = \psi_{11}^{(\text{ZRS})}. \quad (31)$$

We will term this the *zero-Reynolds-stress approximation* (ZRS).

B. Simplified zero-Reynolds-stress approximation

Examining individual terms in $\psi_{11}^{(2)}$, we find for $H \geq 0.7$ and $10^{-2} \leq \beta \leq 10^3$ that $b_1^{(n)} \ll 1$, $b_3^{(n)} \ll 1$, and $b_4^{(n)} \ll 1$, while $b_2^{(n)} \rightarrow i\alpha_n^2 \nu_n k / 4n$. Thus, over this range of H and β , the ZRS approximation can be simplified to yield

$$\psi_{11}^{(s)} \approx \psi_{11}^{(\text{SRS})} = \sin(kx) \sum_{n=1}^{\infty} (b_2^{(n)} + b_2^{(n)*}) \bar{y} \exp(-q\bar{y}). \quad (32)$$

Considering briefly the accuracy of this approximation, we observe that at $\beta=1$ and over $0.7 \leq H \leq 2$, the maximum relative error E between $\psi_{11}^{(\text{SRS})}$ and $\psi_{11}^{(s)}$ (evaluated at 100×100 equally spaced points over $0 \leq x \leq 1$, $0 \leq y \leq H$, and at increments $\Delta H = 0.25$), does not exceed 1.6%. Similar accuracy is generally observed at $\beta = 0.01, 0.1, 10, 100$, and 1000 , and over the same range of H . It should be noted, however, that at certain values of β and H , E can be as high as 220%; visual comparisons of associated streamline patterns suggest that the overall agreement between $\psi_{11}^{(\text{SRS})}$ and $\psi_{11}^{(s)}$ is nevertheless satisfactory. We will refer to this as the *simplified zero-Reynolds-stress approximation* (SRS).

C. Semi-infinite domain approximation

A third approximation to $\psi_{11}^{(s)}$, strictly valid when the fluid layer extends an infinite distance above a single oscillating boundary, can be obtained by replacing the boundary conditions in Eqs. (11) and (12) with

$$\psi_{I,J} \rightarrow 0, \quad y \rightarrow \infty \quad (33)$$

for $I, J = 0, 1$, or, equivalently, by allowing $H \rightarrow \infty$ in Eq. (26). In either case, the steady second-order solution is given by

$$\psi_{11}^{(s)} \approx \psi_{11}^{(\text{SID})} = -\sin(kx) \frac{\beta k}{\sqrt{8}} y e^{-ky} \sum_{n=1}^{\infty} \left(\frac{a_n^2}{\sqrt{n}} \right) \quad (34)$$

(where, for later use, the identity $ky = q\bar{y}$ has been used). The accuracy of this approximation is comparable to that of the SRS approximation. For example, while the maximum relative error at $\beta=1$ and $H=0.7$ is relatively high, approximately 70%, the approximation improves dramatically with increasing gap height H ; E decreases from 19% at $(\beta, H) = (1, 1)$ to 0.83% at $(\beta, H) = (1, 3)$. Similar trends are generally observed at $\beta = 0.01, 0.1, 10, 100$, and 1000 . Again, visual comparisons suggest that the approximation is reasonable even when E is large. We will refer to this as the *semi-*

infinite domain approximation (SID); as with the SRS approximation, the SID approximation can be used for $H \geq 0.7$ and $10^{-2} \leq \beta \leq 10^3$.

V. RESULTS AND DISCUSSION

We will first focus on flows produced by single-boundary forcing, briefly examining the effects of gap height H and Stokes layer thickness (as embodied in) β on second-order flow structure. As a prelude to future studies focused on scalar transport, we will also consider the effect of driving wave form on second-order flow, examining the flow's response to sinusoidal, sawtooth, and square-wave forcing. We then turn to flows produced by dual-boundary forcing, investigating the effects of H , β , the frequency ratio γ , and the upper boundary offset ϕ on second-order flow structure. Where appropriate, we compare the approximate solutions described above with the full second-order asymptotic solution in Eq. (26). Finally, in the next section, we examine particle transport associated with superposed, quasistatic boundary oscillations.

Prior to discussing the results, we note that the flow between two opposing wall wavelengths (possibly offset by distance ϕ) can be mapped to a torus T^2 . Poincaré's index theorem [16], relating the number hyperbolic (saddle) (N_h), elliptic (center) (N_e), and parabolic (N_p) critical (stagnation) points on the torus, is thus given by $N_e - N_h - N_p / 2 = 0$. All steady second-order flows, regardless of the magnitudes of β , H , ϕ , and γ are found to satisfy this relationship.

A. Parametric effects on second-order flow structure: single-boundary forcing

As demonstrated in the next section, studying flow structure (i.e., the distribution of critical points and the arrangement of interconnecting separatrix streamlines) and investigating changes to this structure due to changing flow parameters provide an essential bridge to understanding flow and transport phenomena in low-Reynolds-number flow. In the case of single-boundary forcing, second-order flow structure is determined by three parameters, H , β , and ϕ . Here, we limit attention to the case where the offset ϕ between the upper and lower boundaries is zero. The bifurcation diagram in Fig. 2, obtained for zero offset, shows that over most of the computationally accessible parameter space, the second-order flow is characterized by two counter-rotating cells. Four-cell flows, by contrast, while appearing over a relatively wide range of H , are limited to a small range of β . [Note that round-off error (64-bit precision) becomes significant for $H \geq 5.5$ and $H \leq 0.01$. Thus, calculated results described below are limited to $0.01 \leq H \leq 5.5$.]

As a point of reference, we note that four-cell flows are characterized by three hyperbolic points (per wall wavelength), located at the intersection of separatrix streamlines separating each cell, six parabolic points (per wall wavelength), located at the corners and midpoints of the upper and lower boundaries, and four elliptic points, located at the nominal center of each cell. Refer to Fig. 3. In the case shown ($\phi=0$), three vertical separatrices connect opposing pairs of parabolic points, with separation occurring at $(x, y) = (0, 0)$, $(\frac{1}{2}, H)$, and $(1, 0)$, and reattachment occurring at the

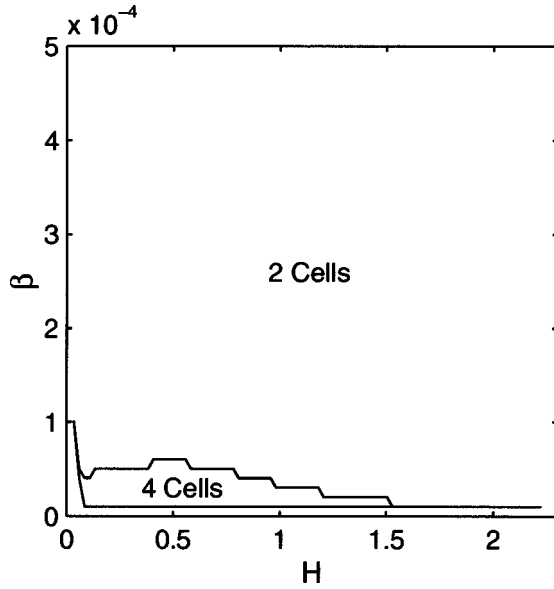


FIG. 2. Bifurcation diagram for flow driven by a single boundary. Wall offset $\phi=0$.

other three points. In slight contrast, two-cell flows contain no hyperbolic points, six parabolic points (all located at the same points on the upper and lower boundaries), and two elliptic points. (Note that hyperbolic points are unresolved in Fig. 3. Also note that the indices for corner parabolic points are effectively equal to $\frac{1}{4}$. This reflects the fact that in mapping the flow to a torus, the boundary at $x=N$ maps to the boundary at $x=N+1$. See Ref. [15] for further discussion and for a description of critical points in two-dimensional flows.)

The first significant finding is that four-cell flow does not have the same physical origin as four-cell flow observed in the low- ϵ limit treated by Lyne [3]. In the latter case (and in the high- Re_s limit), four-cell patterns are produced by non-negligible velocities at the edge of thin Stokes layers. Here, the origin of four-cell patterns becomes apparent when $\psi_{11}^{(1)}$, $\psi_{11}^{(2)}$, and $\psi_{11}^{(s)}$ are plotted across the channel on $x=0.25$; refer to Fig. 3. Since $\psi_{11}^{(1)}$ corresponds to the flow component produced by steady Reynolds stresses while $\psi_{11}^{(2)}$ is the component produced by boundary forcing, then it is clear that four-cell flow appears when both components are of comparable magnitude. In contrast, a similar comparison (not shown) demonstrates that two-cell flow exists when $\psi_{11}^{(2)} \gg \psi_{11}^{(1)}$. [In cases where the offset between the upper and lower boundaries is zero, $\psi_{11}^{(s)}$ has the form $\psi_{11}^{(s)} = \sin(kx)G(y)$. Thus, plots like those in Figs. 3(b) and 3(d) provide a complete description of the second-order flow structure.]

The next important set of findings, applicable under low-Reynolds-stress conditions, concerns the insensitivity of second-order flow structure to fluid layer thickness, Stokes layer thickness, and forcing wave form. The first two results are discussed in this subsection, and the last, which also holds when Reynolds stresses are non-negligible, is described in the next subsection. Figure 4 summarizes the first result, showing that over $H \geq 0.7$, the relative vertical position of elliptic points (y_c/H) satisfies $y_c/H = 1/(2\pi H)$. We can use either the SRS or SID approximations, Eq. (32) or

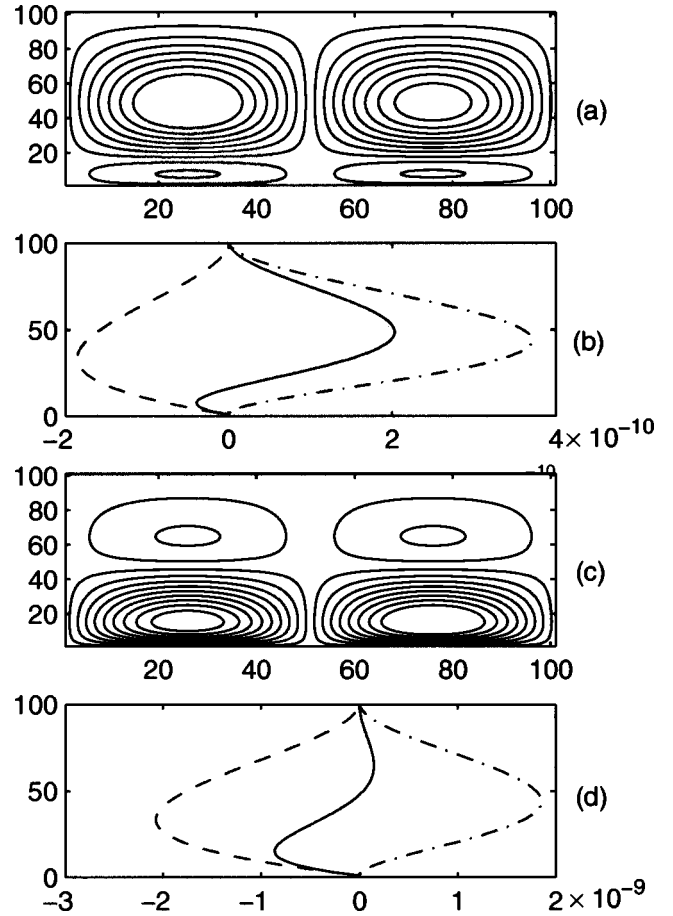


FIG. 3. Typical four-cell flows, single-boundary forcing. Plots (b) and (d) show stream function components on $x=0.25$: $\psi_{11}^{(s)}$ solid line; $\psi_{11}^{(1)}$, dash-dotted line; $\psi_{11}^{(2)}$, dashed line. $\beta=10^{-5}$ in (a) and (b) and 5×10^{-5} in (c) and (d). $H=0.2$ in all four plots. Note that in the streamline plots (a) and (c) the direction of fluid flow is clockwise in left, lower primary cells and counterclockwise in right, lower primary cells. Similar flow patterns hold in all subsequent plots. For convenience in plotting, the abscissas and ordinates on most streamline plots have been rescaled by factors of 100 and $100/H$, respectively.

(34), respectively, to explain this result. Using the SRS approximation, we see that, since the vertical velocity component equals zero on $x=\frac{1}{4}$ and $x=\frac{3}{4}$, elliptic points appear at points on these lines where $\partial_y \psi_{11}^{(s)} \approx \partial_y \psi_{11}^{(SRS)} = 0$, i.e.,

$$\partial_y \psi_{11}^{(SRS)} = \sin(kx_0) \sum_{n=1}^{\infty} (b_2^{(n)} + b_2^{(n)*}) e^{-ky} (1 - ky) = 0, \quad (35)$$

where $x_0 = \frac{1}{4}$ or $\frac{3}{4}$. Thus, approximate center locations appear at

$$y_c = k^{-1} = \frac{1}{2\pi}. \quad (36)$$

The same result follows using the SID approximation, Eq. (34).

The second result is summarized in Fig. 5 where it is shown that over a fairly large portion of the parameter space, $10^{-2} \lesssim \beta$ and $0.2 \lesssim H \lesssim 5.5$, second-order flow structure is

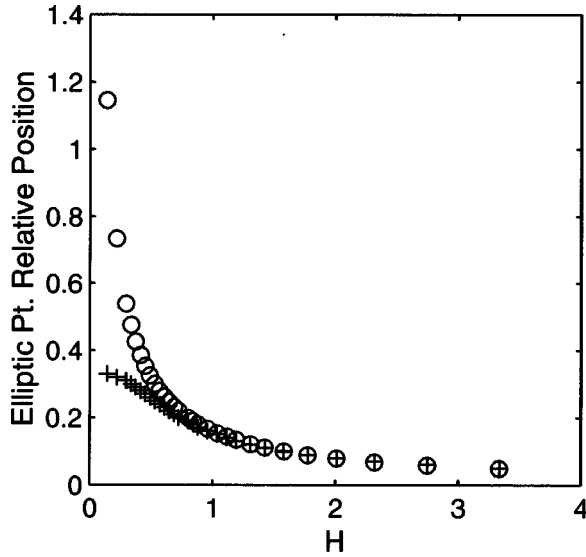


FIG. 4. Flow structure during single-boundary forcing under low-Reynolds-stress conditions ($\psi_{11}^{(2)} \gg \psi_{11}^{(1)}$)—effect of fluid layer thickness H . Comparison plots show relative elliptic point locations (y_c/H) predicted by $\psi_{11}^{(s)}$ (+++) and $\psi_{11}^{(SRS)}$ (or equivalently $\psi_{11}^{(SID)}$) (○○○). Here, $x=0.25$, $\phi=0$, and $\beta=1$.

also independent of the Stokes layer thickness β (results for $H > 3.5$ and $\beta > 1$ are not shown). This result is explained by noting that, over this range of parameters, $\psi_{11}^{(s)}$ is again well approximated by Eq. (31). Inspection of $b_1^{(n)} - b_4^{(n)}$ then shows that $b_1^{(n)}$ and $b_3^{(n)}$ are proportional to β while $b_2^{(n)}$ and $b_4^{(n)}$ are proportional to $\beta^{1/2}$. Thus, since a factor β multiplies all terms in $\psi_{11}^{(2)}$, the condition defining the vertical position of elliptic points, $\partial_y \psi_{11}^{(s)} \approx \partial_y \psi_{11}^{(2)} = 0$ (on $x = \frac{1}{4}$ and $\frac{3}{4}$) is independent of β . This feature is also consistent with the SRS and SID approximations, Eqs. (32) and (34), respectively, which also show that $\psi_{11}^{(SRS)}$ and $\psi_{11}^{(SID)}$ are proportional to β .

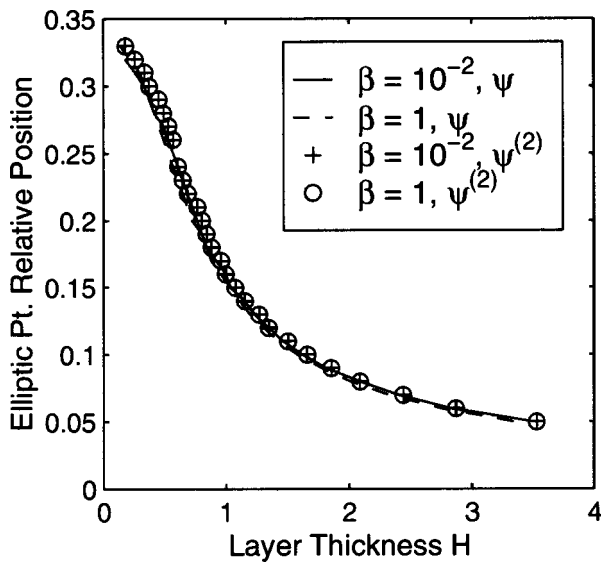


FIG. 5. Flow structure during single-boundary forcing under low-Reynolds-stress conditions ($\psi_{11}^{(2)} \gg \psi_{11}^{(1)}$)—effect of Stokes layer thickness β . Comparison plots show relative elliptic point locations (y_c/H) predicted by $\psi_{11}^{(s)}$ and $\psi_{11}^{(ZRS)}$. Here, $x=0.25$ and $\phi=0$.

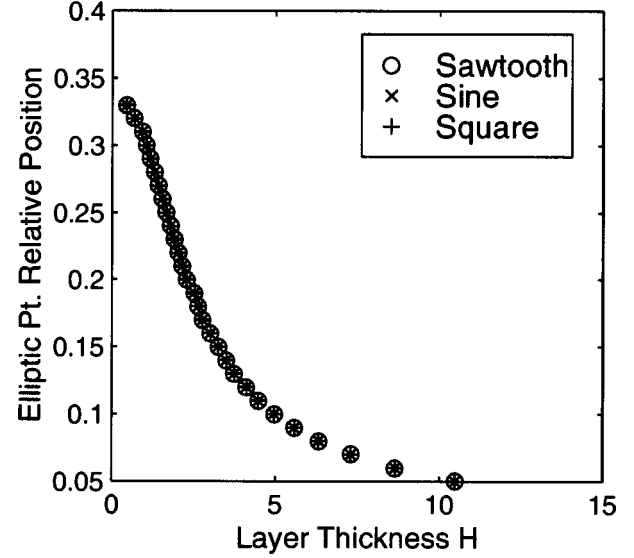


FIG. 6. Effect of forcing wave form on flow structure. Relative elliptic point positions shown along $x=0.25$ with $\beta=1$ and $\phi=0$. Single-boundary forcing.

Representative comparisons of the SRS (or equivalently, the SID) and ZRS approximations with the full second-order solution (26) are shown in Figs. 4 and 5, respectively. All three approximations provide comparable accuracy under the conditions shown. Note that in the case of single-boundary-driven flow none of these approximations predicts four-cell flow, since, as mentioned, four-cell flow reflects a balance between the Reynolds stress flow component $\psi_{11}^{(1)}$ and the boundary-forced component $\psi_{11}^{(2)}$. (See below for full flow field comparisons during dual-boundary forcing.)

B. Effect of forcing wave form

Here we investigate the effect of boundary-forcing wave form on the structure of the second-order flow. While our methods are based on those described in [15,17], it appears that the effect of forcing wave form on *second-order* Stokes flow has not been considered. For single-boundary forcing, the leading order boundary velocity can be written as

$$u_{00} = \epsilon_a F'_a(t) \quad (37)$$

where $F'_a(t)$ represents a boundary velocity wave form and ϵ_a is a normalizing parameter designed to isolate wave form effects. Following Swanson [17] and Jana, Metcalfe, and Ottino [15], we investigate the effect of sinusoidal, sawtooth, and square-wave forcing using two of the three methods they describe: (i) choose each ϵ_a so that all three wave forms have equal average deviation from the mean boundary velocity (which is zero in the present case); and (ii) choose ϵ_a so that the leading term in the Fourier expansion of each wave form is identical. See [15] for further details.

Examining flows over a wide range of H and β , including regimes where Reynolds stresses are non-negligible, we find that the forcing wave form has no observable effect on steady streaming patterns. Figure 6 shows a representative result in the case where Reynolds stresses are small ($\beta = 1$). This finding is consistent with theoretical and experi-

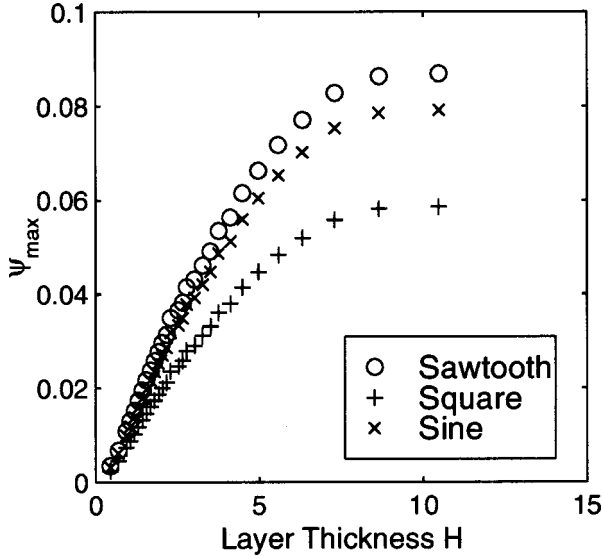


FIG. 7. Effect of forcing wave form on maximum value of $\psi_{11}^{(s)}$. Single-boundary forcing with $\beta=1$ and $\phi=0$.

mental observations of complex non-second-order Stokes flows within driven circular and rectangular cavities [15], and is also consistent with Swanson's [17] computational study of eccentric cylinder flow. While Jana, Metcalfe, and Ottino [15] provide a semiquantitative explanation for this result, here, in cases where Reynolds stresses are negligible, we can pinpoint the exact cause. When $\psi_{11}^{(2)} \gg \psi_{11}^{(1)}$, we can approximate $\psi_{11}^{(s)}$ as $\psi_{11}^{(2)}$ and thus express $\psi_{11}^{(s)}$ in the form

$$\psi_{11}^{(s)} \approx \sin(kx) \sum_{n=1}^{\infty} \{a_n^2 [f_n^{(1)}(H)g_n^{(1)}(y) + f_n^{(2)}(H)g_n^{(2)}(y) + f_n^{(3)}(H)g_n^{(3)}(y) + f_n^{(4)}(H)g_n^{(4)}(y)]\}, \quad (38)$$

where $a_n^2 f_n^{(1)} = (b_n^{(1)} + b_n^{(1)*})$, $a_n^2 f_n^{(2)} = (b_n^{(2)} + b_n^{(2)*})$, $a_n^2 f_n^{(3)} = (b_n^{(3)} + b_n^{(3)*})$, $a_n^2 f_n^{(4)} = (b_n^{(4)} + b_n^{(4)*})$, $g_n^{(1)} = \exp(-ky)$, $g_n^{(2)} = \sqrt{\beta}y \exp(-ky)$, $g_n^{(3)} = \exp(ky)$, and $g_n^{(4)} = \sqrt{\beta}y \exp(ky)$, and where a_n is the n th Fourier coefficient in the expansion for $F'(t)$. It is readily shown that $f_n^{(1)} - f_n^{(4)}$ do not depend on a_n . Thus, since the functions $f_n^{(1)} - f_n^{(4)}$ and $g_n^{(1)} - g_n^{(4)}$ are identical for each wave form, and since the coefficients a_n are multiplied by constant normalization factors, it is clear that over the range of H and β where $\psi_{11}^{(2)} \gg \psi_{11}^{(1)}$, all three wave forms, normalized using either normalization method, will produce essentially identical second-order flow patterns.

While flow structure is independent of wave form, the magnitudes of the streaming velocities induced by each wave form do exhibit slight differences. See Fig. 7 for a representative result. In particular, it is found that the characteristic horizontal velocity between the lowest-lying elliptic points and the forced boundary is highest during sawtooth forcing and lowest during square-wave forcing. This result can be explained, again under typical low-Reynolds-stress conditions, using Eq. (38). Since horizontal (and vertical) velocity components produced by each wave form are proportional to the square of the respective Fourier coefficients a_n , then by comparing dominant first terms we see that

$$\frac{\partial_y \psi_{11}^{(2)}|_{\text{st}}}{\partial_y \psi_{11}^{(2)}|_c} \approx \frac{a_1|_{\text{st}}}{a_1|_c} = \frac{16}{\pi^2} \quad \text{and} \quad \frac{\partial_y \psi_{11}^{(2)}|_{\text{st}}}{\partial_y \psi_{11}^{(2)}|_{\text{sq}}} \approx \frac{a_1|_{\text{st}}}{a_1|_{\text{sq}}} = \frac{8}{\pi},$$

where the subscripts st, c, and sq refer, respectively, to sawtooth, sine, and square-wave forcing.

C. Parametric effects on second-order flow: dual-boundary forcing

We arbitrarily define a reference flow as that corresponding to $H=1.0$, $\gamma=2.0$, $\phi=0.0$, and $\beta=1.0$. Note that the upper and lower boundaries are driven by single frequencies, γ_u and γ_l , respectively, where $\gamma_u/\gamma_l \equiv \gamma$. Also note that when $\phi=0$ wave crests on opposing walls are vertically aligned, while at $\phi=0.5$, crests on one wall are vertically aligned with valleys on the other.

In general, flows forced by both boundaries are sensitive to all flow parameters. Here, we briefly describe structural changes associated with variations in wall offset ϕ , driving frequency ratio γ , and fluid layer thickness H .

1. Variations in wall offset

Comparing representative flow sequences under conditions where the Reynolds stress flow component is negligible and non-negligible (Fig. 8), we see that significant Reynolds stresses ($\beta=10^{-5}$) produce large central cells (one per wall half wavelength). When the Reynolds stress component is small ($\beta=1$), by contrast, no such cells appear and the flow is dominated by boundary-forced cells near each wall. Following [15], we refer to central cells not contacting either boundary as *secondary* cells and cells in direct contact with a boundary as *primary* cells. Although not shown, we note that pairs of flows \mathbf{F}_ϕ and $\mathbf{F}_{-\phi}$, corresponding to equal right and left offsets ϕ and $-\phi$ about $\phi=0$ (or about $\phi=0.50$), are reflectionally symmetric [18] about the y axis to the *time-reversed* flows $\mathbf{F}_{-\phi}^{-1}$ and \mathbf{F}_ϕ^{-1} , respectively (where \mathbf{F}_ϕ^{-1} is obtained from \mathbf{F}_ϕ by multiplying both velocity components in the latter by -1).

2. Driving-frequency variations

As the ratio of driving frequencies γ increases, the flow induced by the higher-frequency boundary begins to dominate that produced by the lower-frequency boundary; refer to Fig. 9. Two observations provide insight into this intuitively reasonable result. First, the second-order tangential velocity at either boundary is proportional to the rate of work done by boundary displacements against leading order viscous shear, i.e., $\partial_y \psi_{11} = -k \sin(kx) F(t) \partial_y^2 \psi_{00}$ (at $y=0$). Since this term is proportional to γ (at the higher-frequency boundary), then so is the associated energy input. Second, since the boundary-forced stream function component $\psi_{11}^{(2)}$ is proportional to $\gamma^{3/2}$ and since $\psi_{11}^{(2)} \gg \psi_{11}^{(1)}$ in the flows depicted in Fig. 9, then the magnitude of the stream function associated with the high-frequency boundary also varies as $\gamma^{3/2}$. A similar result is also observed when β is small, i.e., when Reynolds stresses are significant (result not shown). More generally, flows driven by both boundaries assume the character of single-boundary-driven flows when $\gamma \geq 5$. Finally, note from Fig. 9 that a flow \mathbf{F}_K having $\gamma=K$ is reflectionally symmetric

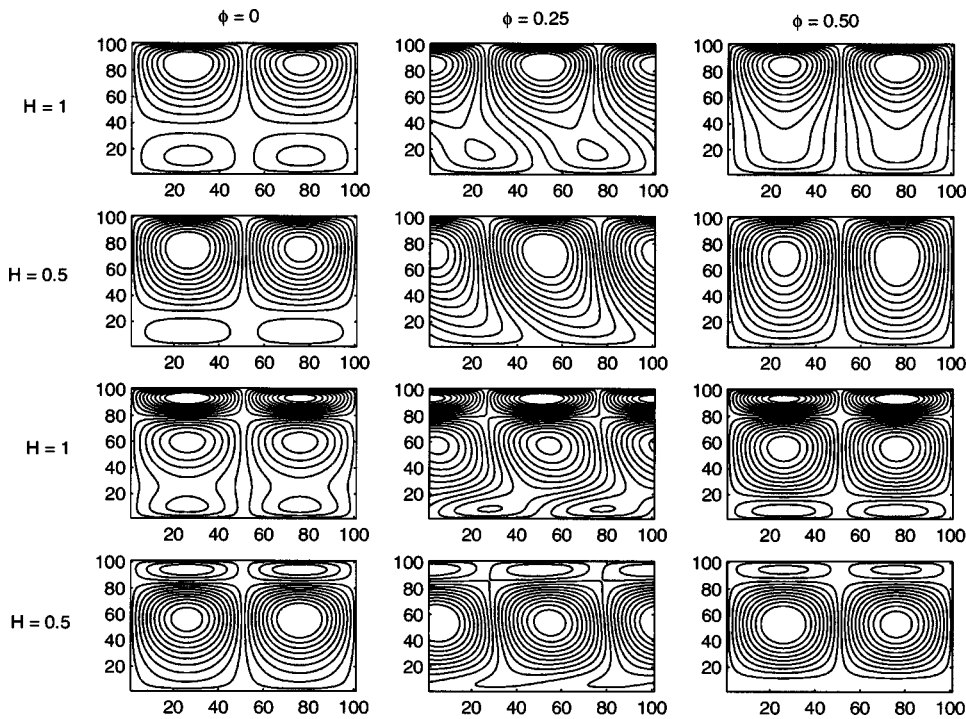


FIG. 8. Effect of Reynolds stresses on dual-boundary-driven flow structure. $\beta=1$ (Reynolds stresses negligible) in the six uppermost plots while $\beta=10^{-5}$ (Reynolds stresses non-negligible) in the lower six plots. $\gamma=2$ in all plots. Flow patterns shown in Figs. 8–10 span the channel in the vertical direction and span one wall wavelength in the horizontal direction. Horizontal and vertical dimensionless length units are scaled by factors of 100 and $100/H$, respectively.

(about the x axis) to the flow $F_{1/K}$ where $\gamma=1/K$ (and where H, ϕ , and β are equal).

3. Channel height variations

As shown in Fig. 10, for $H \geq 1$, two pairs of isolated, apparently noninteracting primary cells appear near each

boundary. For $10^{-1} \leq H \leq 1$ and moderate β , the Reynolds stress component is again negligible and height reductions either eliminate lower primary cells (when $\phi \neq 0$), or in the case $\phi=0$, squeeze them toward the lower boundary (see, e.g., Fig. 8). A similar effect is observed when Reynolds-stress-driven flow is significant ($\beta=10^{-5}$). In this case, depending on the offset, lower primary cells are squeezed or

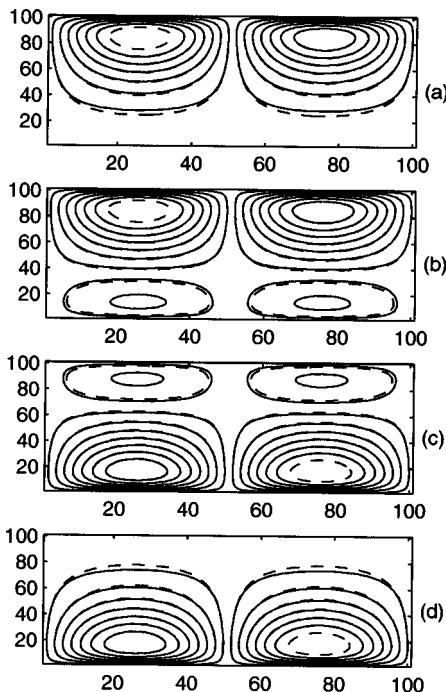


FIG. 9. Effect of frequency ratio γ during dual-boundary forcing—low-Reynolds-stress conditions. Comparison plots show $\psi_{11}^{(s)}$ (solid line) and semi-infinite domain approximation $\psi_{11}^{(SID)}$ (dashed line). Here, $H=1.0, \beta=1.0, \phi=0$, and γ has the following values: (a) 5; (b) 2; (c) $\frac{1}{2}$; (d) $\frac{1}{5}$. See caption to Fig. 8 for explanation of horizontal and vertical length units.

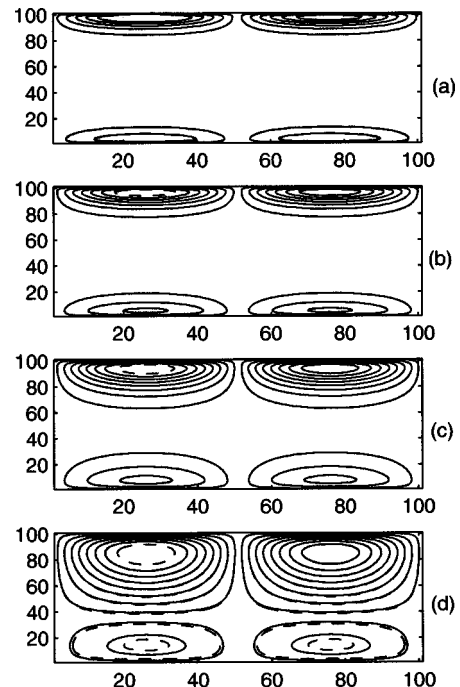


FIG. 10. Effect of fluid layer thickness H during dual-boundary forcing—low-Reynolds-stress conditions. Comparison plots show $\psi_{11}^{(s)}$ (solid line) and semi-infinite domain approximation $\psi_{11}^{(SID)}$ (dashed line). Here $\phi=0.0, \beta=1.0, \gamma=2$, and H has the following values: (a) 5; (b) 3.66; (c) 2.33; (d) 1. See caption to Fig. 8 for explanation of horizontal and vertical length units.

eliminated by central Reynolds-stress-driven (secondary) cells (again, see Fig. 8).

VI. QUASISTATIC FORCING AND LONG-RANGE PARTICLE TRANSPORT

In this final section, we examine qualitative features of particle transport produced by large-scale quasistatic oscillation of either wall, where the slow (quasistatic) oscillation is superposed on the rapid oscillations driving steady streaming flow. A number of studies have examined particle transport associated with unsteady, *nonsecondary* Stokes flows [17,19–22], capillary waves [23,24], traveling waves [25–27], Rossby waves and irrotational flows [28], and water waves [1]. However, it appears that no work has been reported on transport within secondary Stokes flows.

Although beyond the scope of the present paper, quantitative descriptions of particle transport are possible, e.g., using the transport theory developed by Wiggins and co-workers (see, e.g., [29]). Since hyperbolic points clearly oscillate with the quasistatic motion of the upper boundary, manifolds of corresponding fixed points intersect an infinite number of times to form lobes; cycle-to-cycle transport between adjacent cells is comprised of the contents of these lobes [29]. We also note that Ryrie [30] investigated transport in spatially periodic, time-modulated flows and applied the approach described by Rom-Kedar, Leonard, and Wiggins [31] to quantitate the transport.

Here, quasistatic oscillations are produced by slowly varying the wall offset ϕ :

$$\phi(t) = L_0 + L_t \sin(\epsilon_t t), \quad (39)$$

where L_0 is the center of oscillation (measured relative to $x=0$), L_t is the oscillation amplitude, $\epsilon_t = \hat{\omega}_s / \hat{\omega}_f$ is the dimensionless oscillation frequency, and $\hat{\omega}_s$ and $\hat{\omega}_f$ are the dimensional slow and fast oscillation frequencies. Quasistatic conditions prevail when the viscous diffusion time scale is much shorter than the large-scale oscillation period, i.e., when $\hat{\lambda}^2 / \hat{\nu} \hat{T}_s \ll 1$, where $\hat{T}_s = 2\pi / \hat{\omega}_s$. Equivalently, based on definitions given earlier, quasistatic conditions exist if $\epsilon_t \ll 2\pi\beta^{-1}$. This condition is well satisfied here since $\epsilon_t = 1 \times 10^{-9}$ while $\beta = 10^{-5}$. Particle paths are calculated by integrating the following system via a fourth-order Runge-Kutta scheme:

$$\dot{x} = \partial_y \psi_{11}(x, y, z), \quad \dot{y} = -\partial_x \psi_{11}(x, y, z) \quad \text{where } \dot{z} = \epsilon_t. \quad (40)$$

Initially, an array of 1024 particles is distributed uniformly over $0 \leq x \leq 1$, $0 < y < H$; the position of each particle is then determined at 5000 equal time increments Δt , where $\Delta t = 1.818 \times 10^6$ and where one quasistatic oscillation period equals $550\Delta t$.

Flow patterns and particle positions shown correspond to those extant over one or more wall wavelengths. (Note that, over the N th wavelength on the lower boundary, $N \leq x < N + 1$.) Hereafter, the leftmost and rightmost central (secondary) cells in wavelength N will be referred to as LC(N) and RC(N), respectively; when portions of three central cells are present, the middle cell will be referred to as MC(N). *Upper boundary cells* are smaller primary cells located between

central cells and the upper boundary; each of these occupies about 20% of the channel width and will be similarly denoted as LB(N), MB(N), and RE(N). Likewise, lower boundary cells are located between central cells and the lower boundary and will be denoted as LBI(N), MBI(N), and RBI(N).

A. Bifurcations leading to long-range transport

We define long-range particle transport as transport occurring over more than one wall wavelength. Although numerous computational experiments have been performed, we focus on representative results obtained under one set of conditions: $\beta = 10^{-5}$, $H = 1$, $\gamma = 2$. The short-time and asymptotic transport characteristics described below are observed for $10^{-5} \leq \beta \leq 10^{-4}$, $0.3 \leq H \leq 2$, and $\frac{1}{4} \leq \gamma \leq 4$.

Importantly, we find that long-range transport is possible only under the following conditions: (1) the Reynolds-stress-induced flow component must be comparable to or much larger than the boundary-forced component, and (2) the pair of bifurcations depicted in Fig. 11 must occur. Referring to Fig. 11, we see that the flow undergoes two bifurcations as the wall offset passes through $\phi = 0.5$. When $\phi = 0.49$, stagnation streamlines connecting parabolic points on opposing boundaries form a right-running stair-step pattern (from bottom to top) across the channel. We will refer to these as cross-channel stagnation streamlines (CCSL's). Notice that limited flow can occur between each trio of cells encompassed by adjacent CCSL's. Note too that connected pairs of parabolic points are essentially one wall wavelength out of phase. When $\phi = 0.50$, the unresolved hyperbolic points in Fig. 11(a) shift slightly rightward to $(x, y) = (0.5, 0.8)$ and $(x, y) = (0.5, \approx 0.17)$, and all intercellular flow ceases. Finally, when $\phi = 0.51$, cross-channel stagnation streamlines form a *left-running* stair-step pattern between lower and upper parabolic points, and flow can again take place between enclosed trios of cells. Again, pairs of connected parabolic points are essentially one wavelength out of phase. Taken together, we see that this pair of bifurcations results in stagnation streamlines ‘‘hopping’’ two wavelengths along a boundary, effectively closing one cross-channel flow path while opening another. Indeed, this bifurcation pair constitutes the key mechanism underlying long-range transport.

B. Short-time transport

We arbitrarily define early- or short-time transport as transport occurring over $0 < t < 750\Delta t$, or transport occurring over approximately one slow oscillation period. Under most conditions, the uniform array of particles immediately breaks up into two large, centrally located particle clouds and at least two smaller clouds near the upper boundary. As indicated in Figs. 12(a) and 12(c), breakup occurs along separatrix streamlines between neighboring cells. (Note that quasistatic boundary motion is left to right in Fig. 12.) Due to the bifurcations at $\phi = 0.5$, particles in central cells gradually leak into neighboring lower boundary cells and then undergo filamentary transport on the periphery of adjacent central cells.

Filamentary motion is mediated by two mechanisms. First, the bifurcations at $\phi = 0.5$ effectively switch one set of

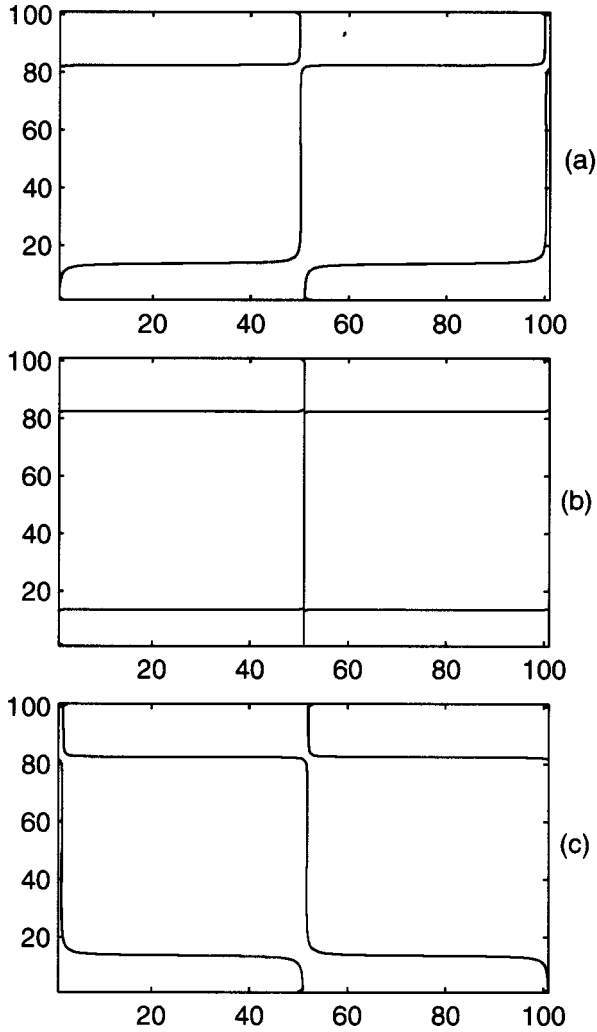


FIG. 11. Flow bifurcations as wall offset passes through $\phi = 0.5$. Cross-channel streamlines are shown with $\beta = 10^{-5}$, $H = 0.85$, and $\gamma = 2$. ϕ has the following values: (a) 0.49; (b) 0.50; (c) 0.51. Notice that at $\phi = 0.49$ mass transport can occur between the lower primary cell on the left, the central cell on the right, and, to a lesser extent, the upper primary cell located to the right of the right central cell. All intercellular transport paths are closed at $\phi = 0.5$, but reopen at $\phi = 0.51$ as shown in (c). Horizontal and vertical dimensionless length units are scaled by factors of 100 and $100/H$, respectively.

CCSL's with another, closing the path between $LB(N)$, $MC(N)$, and $RBI(N)$ and opening a path between $RB(N)$, $MC(N)$, and $LBI(N)$. Second, after traveling around the periphery of a given central cell, particles accumulate in low-speed, lower primary cells and in the relatively slow-moving lower reaches of central cells. The accumulated particles then appear to serve as secondary particle sources for the extending filament. [Note, just as left-to-right (LTR) quasistatic boundary motion induces leftward filamentary particle transport, right-to-left (RTL) boundary motion produces rightward filamentary transport (results not shown).]

Filamentary transport along cell boundaries has also been observed by Moses and Steinberg [26] in traveling waves. As in the present case, they observe filamentary motion ("backflow") in a direction opposite the wave vector and collective particle motion in the direction of wave propaga-

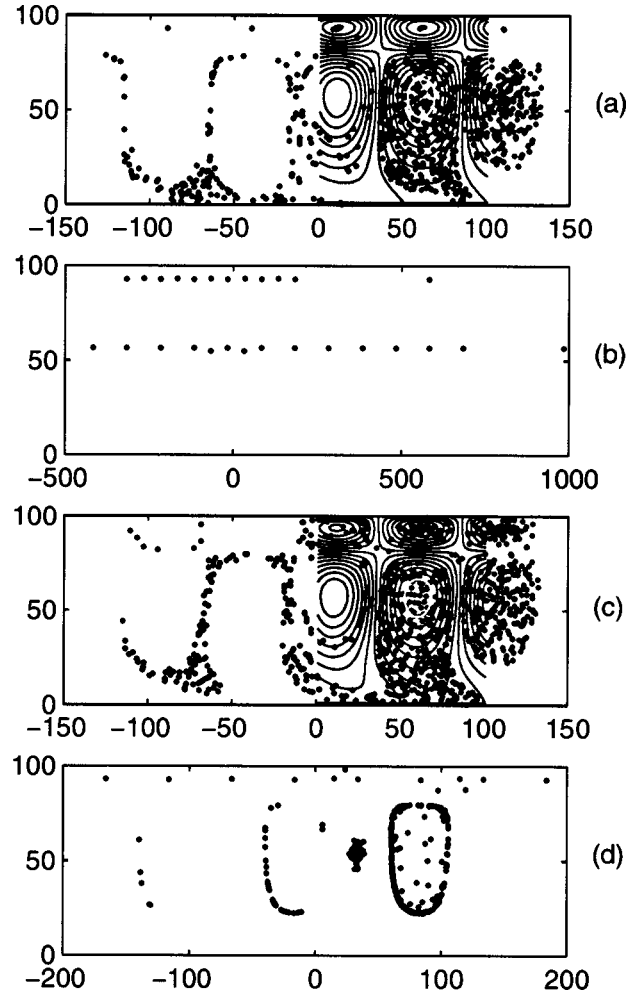


FIG. 12. Particle transport characteristics with $\beta = 10^{-5}$, $H = 0.85$, $L_0 = 0.5875$, and $L_t = 0.6$. Elapsed times equal $40\Delta t$ in (a) and (b) and $4950\Delta t$ in (c) and (d). $\gamma = 4$ in (a),(b) and 3 in (c),(d). Horizontal and vertical dimensionless length units are scaled by factors of 100 and $100/H$, respectively.

tion. Using Eqs. (28) and (39) and noting that $\epsilon_t t \ll 1$ during initial LTR (or RTL) boundary motion, we can readily express the stream function associated with upper-boundary motion in traveling wave form, $\psi_{11}^u = \sin(kx - \omega t - \phi_u)F(y)$, where $\omega = L_t \epsilon_t$ and $\phi_u = 1 + L_0$, and where $F(y)$ follows from the solution for $\psi_{11}^{(su)}$. Thus, as is intuitively obvious, rightward (or leftward) quasistatic boundary motion introduces a traveling wave mode into the second-order flow.

Minimal transport occurs between central cells and upper primary cells during the early period. Particles initially located in upper primary cells experience intense mixing and rapid agglomeration toward each cell's instantaneous elliptic point. Particles within central cells, by contrast, remain relatively undisturbed and confined to the central region through $t \approx 750\Delta t$. Inspection of streamline patterns similar to those shown in Fig. 11 (but encompassing $0 \leq \phi \leq 1.0$) clearly shows that for all offsets ϕ , two structural features engender poor transport to or from upper boundary cells: (1) a CCSL *always* separates any given upper primary cell from the central cell immediately below, and (2) the distance between pairs of neighboring CCSL's (measured normal to either CCSL) reaches a minimum at a point between any given

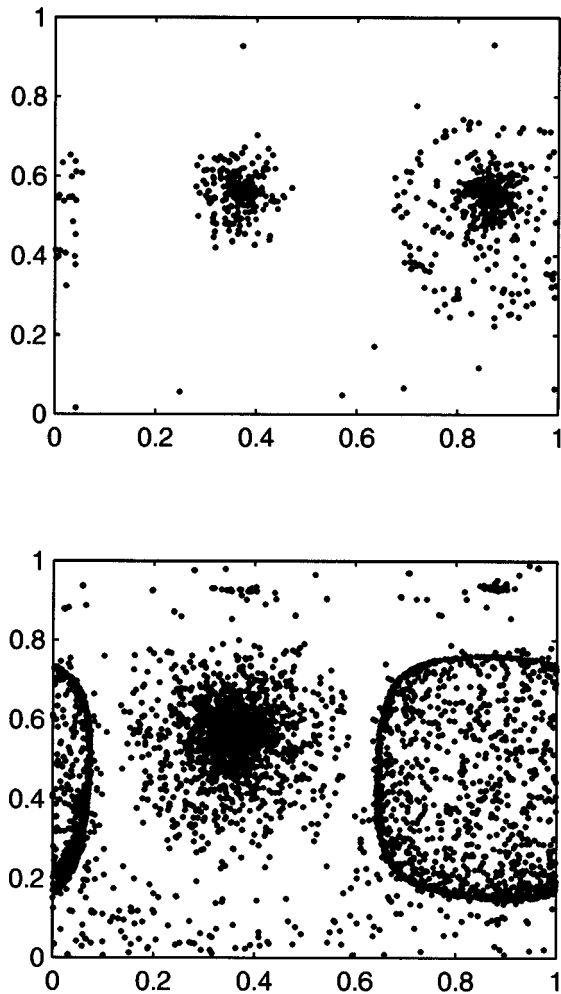


FIG. 13. Poincaré sections. Dimensionless lengths are shown on the horizontal axis while dimensionless lengths on the vertical axis are scaled by a factor of $1/H$.

central cell and the upper primary cell located above and to the right (when $\phi < 0.5$) (or when $\phi > 0.5$, between a central cell and the upper primary cell located above and to the left).

C. Asymptotic transport

Under all conditions tested, particles either accumulate (agglomerate) near, or move away from, oscillating elliptic points in the flow [see Figs. 12(b) and 12(d)]. Indeed, *complete* agglomeration at elliptic points is observed at high driving frequencies, as shown in Fig. 12(b) ($\gamma=4$). (Note that all 1024 particles have accumulated at the elliptic points shown.) When $\gamma=3$, particles both agglomerate at elliptic points *and* collect on the periphery of central cells [see Fig. 12(d)]; similar behavior is observed when oscillation amplitudes L_i are relatively small, on the order of 0.15 or less (result not shown).

Asymptotic transport can be usefully characterized by examining Poincaré sections. Here, Poincaré maps showing the positions of all 1024 particles at the end of each slow (quasi-static) oscillation period are determined by mapping particle positions above any wall wavelength N to the region above the first wavelength, $0 \leq x < 1$, $0 \leq y \leq H$. This is equivalent to determining Poincaré maps on the torus T^2 . (Mapping positions of all particles proves much more infor-

mative than mapping limited numbers of particles. Typically, individual particle motion becomes periodic and corresponding Poincaré maps reveal little concerning overall transport characteristics.) The Poincaré map corresponding to Fig. 12(b), shown at the top of Fig. 13, reveals that agglomeration within central and upper boundary cells corresponds to attraction toward period-1 elliptic points. [Note that the central, left-lying period-1 point indicated in the upper map in Fig. 13 corresponds to oscillating elliptic points in left central cells $LC(N)$ while the right period-1 point corresponds to oscillating elliptic points in right central cells $RC(N)$.]

The Poincaré map corresponding to Fig. 12(d), shown at the bottom of Fig. 13, indicates that asymptotic particle motion toward, then on, the periphery of central cells corresponds to attraction toward a limit cycle. The limit cycle encompasses a period-1 point in the right central cell, where again the fixed point corresponds to oscillating elliptic points in $RC(N)$. Notice that existence of limit cycles is clearly indicated in Fig. 12. It is found that particles on the interior of the limit cycle gradually migrate outward onto the cycle while nearby outlying particles migrate inward; additionally, individual particle trajectories on the limit cycle are purely periodic, having the same period as the slow oscillation. As in the previous case (where $\gamma=4$), particle agglomeration occurs in a number of upper boundary cells, while agglomeration within central cells is limited to $LC(1)$. Again, agglomeration corresponds to attraction toward period-1 elliptic points. Although not shown, under certain conditions, particles are repulsed by central elliptic points; this corresponds to repulsion from unstable period-1 points.

It appears that neither particle accumulation mechanism (i.e., accumulation at fixed points and on limit cycles) has been identified in the particle agglomeration literature. We note that these mechanisms are purely kinematic (i.e., particle velocities are at all times equal to the local fluid velocity) and thus are most likely realized when fluid viscous forces on each particle dominate particle inertial and buoyancy forces and interparticle collisional momentum transfer.

In closing, we note that, unlike particle transport in other systems, long-range transport here is not mediated by particle trapping within translating heteroclinic orbits [25,26,28] and does not require molecular diffusion [32]. To the contrary, long-range transport in this system requires bifurcation of CCSL's as shown in Fig. 11.

VII. SUMMARY AND CONCLUSIONS

A model, applicable in the low streaming Reynolds number limit, has been developed to describe second-order streaming in an oscillating wavy-walled channel. In contrast to earlier studies [3–5], the present model considers flow driven by moving boundaries and is thus subject to a nonhomogeneous second-order boundary velocity condition. Due to this condition, the steady second-order flow is driven by a combination of steady Reynolds stresses within the flow and boundary forcing. Under most conditions, the boundary-forced flow component dominates the Reynolds stress component; Reynolds-stress-driven flow becomes important only when the characteristic Stokes layer thickness becomes much larger than the wall wavelength ($\beta \ll 1$).

Under single-boundary forcing, the flow can have a two-

or four-cell structure (per wall wavelength). Two-cell flow exists for all computationally realizable channel heights ($0.1 \leq H \leq 5.5$) and $\beta \geq 10^{-4}$, while four-cell flow exists for $0.1 \leq H \leq 2.3$ and $\beta \leq 10^{-4}$. The physical origin of four-cell flow in the present model differs completely from the well-known mechanisms driving four-cell flow in oscillatory flow past a stationary wavy wall [3]. Here, four-cell flow arises due to competition between the boundary-forced and Reynolds-stress-driven flow components; four-cell flow never occurs when the boundary-forced component is dominant.

Three approximations, valid under low-Reynolds-stress conditions, are derived and compared against the full second-order solution. For all computationally realizable frequency ratios γ , all wall offsets ϕ , and over the ranges $H \geq 0.7$ and $10^3 \geq \beta \geq 10^{-2}$, all three provide reasonable approximations to the full asymptotic solution (under both single- and dual-boundary forcing).

During single-boundary forcing and under typical low-Reynolds-stress conditions, flow structure is independent of the fluid layer thickness, the Stokes layer thickness, and the forcing wave form. The last result is consistent with observations in non-second-order Stokes flow [15] and can be quantitatively explained by noting that each wave form leads to a solution of the form $\psi = f(x) \sum_{n=1}^{\infty} [a_n^2 F_n(H, y)]$. Since each solution differs only in the form of the Fourier coefficients a_n , differences between solutions become negligible when the coefficients are normalized as described above. Similar arguments, based on the approximations given above, are used to explain the first two results as well.

In contrast to single-boundary-driven flow, flow structure produced by dual-boundary forcing is sensitive to all flow parameters, including fluid layer thickness, the offset between opposing walls, the ratio of frequencies driving both boundaries, and the Stokes layer thickness. It is found that, as the frequency ratio γ increases, the flow becomes increasingly determined by the higher-frequency boundary; dual-boundary flow assumes the character of single-boundary-

driven flow for $\gamma \geq 5$ (or, equivalently, for $\gamma \lesssim \frac{1}{5}$). Structural differences between flows in which Reynolds stresses are negligible and non-negligible are also highlighted. Here we find that, as β decreases below 10^{-4} , Reynolds-stress-driven central (secondary) cells emerge and squeeze near-boundary (boundary-forced) primary cells toward each wall. At larger values of β , Reynolds stresses are negligible, central cells are suppressed, and the flow is dominated by boundary-forced, near-boundary cells.

Finally, we investigate particle transport produced by superposed large-scale quasistatic oscillations of one boundary. Long-range transport occurs only when the Reynolds-stress-driven flow component is comparable to the boundary-forced component and, further, requires two bifurcations of cross-channel stagnation streamlines. The bifurcations occur when crests pass through vertical alignment with opposing valleys and are characterized by pairs of CCSL's effectively "hopping" two wavelengths along either boundary. Short-time transport is characterized by collective particle motion in the direction of quasistatic boundary displacement and filamentary motion in the opposite direction, features consistent with transport in traveling waves [26]. Asymptotic particle transport is dominated by three processes: (i) attraction toward stable period-1 elliptic points, (ii) attraction toward limit cycles, and (iii) repulsion from unstable period-1 elliptic points. These features apparently have not been reported in previous particle transport studies.

ACKNOWLEDGMENTS

Comments provided by Professor Robert E. Johnson are gratefully acknowledged. This work was supported by the National Science Foundation, Grant No. DMI-9712818.

APPENDIX: COEFFICIENTS IN LEADING AND HIGHER-ORDER SOLUTIONS

The coefficients \tilde{A}_n , \tilde{B}_n , \tilde{C}_n , \tilde{D}_n , \tilde{E}_n , and \tilde{F}_n appearing in the $O(\epsilon_w)$ solution (20) are given as follows:

$$A_4^{(n)} = \frac{\{\nu_n(B_n - A_n)(\omega_n \tilde{B}_n - \tilde{A}_n \tilde{E}_n / \tilde{C}_n)\}}{\{[(\tilde{D}_n / \tilde{C}_n)(\omega_n - q) - (\omega_n + q)][\omega_n \tilde{B}_n - \tilde{A}_n \tilde{E}_n / \tilde{C}_n] + [(\tilde{A}_n / \tilde{C}_n)(\omega_n - q) - 2\omega_n][\tilde{D}_n \tilde{E}_n / \tilde{C}_n - \tilde{F}_n]\}}, \quad (\text{A1})$$

$$A_3^{(n)} = \frac{\nu_n(B_n - A_n) - A_4^{(n)}[(\tilde{D}_n / \tilde{C}_n)(\omega_n - q) - (\omega_n + q)]}{[(\tilde{A}_n / \tilde{C}_n)(\omega_n - q) - 2\omega_n]}, \quad (\text{A2})$$

$$A_2^{(n)} = -\frac{\tilde{A}_n A_3^{(n)} + \tilde{D}_n A_4^{(n)}}{\tilde{C}_n}, \quad (\text{A3})$$

$$A_1^{(n)} = -(A_2^{(n)} + A_3^{(n)} + A_4^{(n)}), \quad (\text{A4})$$

$$\tilde{A}_n = \exp(-\omega_n \tilde{H}) - \exp(\omega_n \tilde{H}), \quad (\text{A5})$$

$$\tilde{B}_n = \exp(-\omega_n \tilde{H}) + \exp(\omega_n \tilde{H}), \quad (\text{A6})$$

$$\tilde{C}_n = \exp(q \tilde{H}) - \exp(\omega_n \tilde{H}), \quad (\text{A7})$$

$$\tilde{D}_n = \exp(-q\tilde{H}) - \exp(\omega_n\tilde{H}), \quad (\text{A8})$$

$$\tilde{E}_n = \omega_n \exp(\omega_n\tilde{H}) - q \exp(q\tilde{H}), \quad (\text{A9})$$

$$\tilde{F}_n = \omega_n \exp(\omega_n\tilde{H}) + q \exp(-q\tilde{H}). \quad (\text{A10})$$

Here, $q = k/\sqrt{\beta}$ and $\omega_n = \sqrt{k^2/\beta + ni}$.

Coefficients appearing in the $O(\epsilon\epsilon_w)$ solution in Eq. (26) are given below:

$$C_j^{(n)} = \frac{inA_n A_j^{(n)*} \Lambda_j}{(K_{jn}^2 - q^2)^2}, \quad (\text{A11})$$

$$D_j^{(n)} = \frac{inB_n A_j^{(n)*} \Lambda_j}{(M_{jn}^2 - q^2)^2}, \quad (\text{A12})$$

where

$$\log_2 \Lambda_j = \frac{1}{2}[1 + (-1)^{j+1}], \quad j = 1, 2, 3, 4, \quad (\text{A13})$$

$$K_{1n} = \nu_n + \omega_n^*, \quad K_{2n} = \nu_n + q, \quad (\text{A14})$$

$$K_{3n} = \nu_n - \omega_n^*, \quad K_{4n} = \nu_n - q, \quad (\text{A15})$$

$$M_{1n} = -\nu_n + \omega_n^*, \quad M_{2n} = -\nu_n + q, \quad (\text{A16})$$

$$M_{3n} = -\nu_n - \omega_n^*, \quad M_{4n} = -\nu_n - q. \quad (\text{A17})$$

Prior to listing the coefficients $a_1^{(n)} - a_4^{(n)}$, we define the following quantities:

$$D_0 = \{2 \sinh^2(q\tilde{H}) + 2(q\tilde{H})^2 e^{q\tilde{H}} [\sinh(q\tilde{H}) - \cosh(q\tilde{H})]\}, \quad (\text{A18})$$

$$\begin{aligned} N^{(n)} = & q\tilde{H}^2 e^{q\tilde{H}} [\cosh(q\tilde{H}) - \sinh(q\tilde{H})] P_1^{(n)} + e^{q\tilde{H}} \{(q\tilde{H})^2 \sinh(q\tilde{H}) + (1 - q\tilde{H})[q\tilde{H} \cosh(q\tilde{H}) \\ & + \sinh(q\tilde{H})]\} P_2^{(n)} + [\tilde{H} \sinh(q\tilde{H})] P_3^{(n)} - [q\tilde{H} \cosh(q\tilde{H}) + \sinh(q\tilde{H})] P_4^{(n)}, \end{aligned} \quad (\text{A19})$$

where

$$P_1^{(n)} = - \sum_{j=1}^4 (K_{jn} C_j^{(n)} + M_{jn} D_j^{(n)}), \quad (\text{A20})$$

$$P_2^{(n)} = - \sum_{j=1}^4 (C_j^{(n)} + D_j^{(n)}), \quad (\text{A21})$$

$$P_3^{(n)} = - \sum_{j=1}^4 [K_{jn} C_j^{(n)} \exp(K_{jn}\tilde{H}) + M_{jn} D_j^{(n)} \exp(M_{jn}\tilde{H})] \quad (\text{A22})$$

$$P_4^{(n)} = - \sum_{j=1}^4 [C_j^{(n)} \exp(K_{jn}\tilde{H}) + D_j^{(n)} \exp(M_{jn}\tilde{H})]. \quad (\text{A23})$$

Based on these definitions, $a_1^{(n)} - a_4^{(n)}$ and $b_1^{(n)} - b_4^{(n)}$ are given as follows:

$$a_1^{(n)} = \frac{N^{(n)}}{D_0}, \quad (\text{A24})$$

$$a_2^{(n)} = \frac{[2(q\tilde{H}e^{q\tilde{H}} - \sinh(q\tilde{H}))a_1^{(n)} + e^{q\tilde{H}}(1 - q\tilde{H})P_2^{(n)} + \tilde{H}e^{q\tilde{H}}P_1^{(n)} - P_4^{(n)}]}{2\tilde{H} \sinh(q\tilde{H})}, \quad (\text{A25})$$

$$a_3^{(n)} = P_2^{(n)} - a_1^{(n)}, \quad (\text{A26})$$

$$a_4^{(n)} = 2qa_1^{(n)} - a_2^{(n)} + P_1^{(n)} - qP_2^{(n)}, \quad (\text{A27})$$

$$b_1^{(n)} = \frac{ik\sqrt{\beta}}{2n} a_n \nu_n \tilde{H}^2 e^{q\tilde{H}} (B_n - A_n) [\cosh(q\tilde{H}) - \sinh(q\tilde{H})] D_0^{-1}, \quad (\text{A28})$$

$$b_2^{(n)} = \frac{\{2[q\tilde{H}e^{q\tilde{H}} - \sinh(q\tilde{H})]b_1^{(n)} + \tilde{H}e^{q\tilde{H}}(ik\sqrt{\beta/2n})a_n\nu_n(B_n - A_n)\}}{2\tilde{H}\sinh(q\tilde{H})} \quad (\text{A29})$$

$$b_3^{(n)} = -b_1^{(n)}, \quad (\text{A30})$$

$$b_4^{(n)} = 2qb_1^{(n)} - b_2^{(n)} + (ik\sqrt{\beta/2n})a_n\nu_n(B_n - A_n). \quad (\text{A31})$$

- [1] M. S. Longuet-Higgins, *Philos. Trans. R. Soc. London, Ser. A* **245**, 535 (1953).
- [2] R. E. Johnson, *J. Appl. Mech.* **50**, 244 (1983).
- [3] W. H. Lyne, *J. Fluid Mech.* **50**, 33 (1971).
- [4] A. Kaneko and H. Honji, *J. Fluid Mech.* **93**, 727 (1979).
- [5] G. Vittori, *J. Hydraul. Res.* **27**, 267 (1989).
- [6] B. J. Davidson, *Int. J. Heat Mass Transf.* **16**, 1703 (1973).
- [7] A. Gopinath and A. F. Mills, *J. Heat Transfer* **115**, 332 (1993).
- [8] E. H. Trinh and J. L. Robey, *Phys. Fluids* **6**, 3567 (1994).
- [9] J. A. Bowman and D. T. Schwartz, *Int. J. Heat Mass Transf.* **41**, 1065 (1998).
- [10] T. L. Hoffmann and G. H. Koopmann, *J. Acoust. Soc. Am.* **99**, 2130 (1996).
- [11] J. T. Stuart, *J. Fluid Mech.* **24**, 673 (1966).
- [12] N. Riley, *Q. J. Mech. Appl. Math.* **19**, 461 (1966).
- [13] A. Kaneko, *Proc. JSCE* **307**, 113 (1981).
- [14] H. Schlichting, *Phys. Z.* **33**, 327 (1932).
- [15] S. C. Jana, G. Metcalfe, and J. M. Ottino, *J. Fluid Mech.* **269**, 199 (1994).
- [16] L. Perko, *Differential Equations and Dynamical Systems* (Springer-Verlag, New York, 1991).
- [17] P. D. Swanson, Ph.D. dissertation, University of Massachusetts, Amherst, 1991.
- [18] J. G. Franjione, C.-V. Leong, and J. M. Ottino, *Phys. Fluids A* **1**, 1772 (1989).
- [19] H. Aref and S. Balachandar, *Phys. Fluids* **29**, 3515 (1986).
- [20] C. K. Chaiken, C. K. Chu, M. Tabor, and Q. M. Tan, *Phys. Fluids* **30**, 687 (1987).
- [21] W.-L. Chien, H. Rising, and J. M. Ottino, *J. Fluid Mech.* **170**, 355 (1986).
- [22] T. Kaper and S. Wiggins, *J. Fluid Mech.* **253**, 211 (1993).
- [23] R. Ramshankar, D. Berlin, and J. P. Gollub, *Phys. Fluids A* **2**, 1955 (1990).
- [24] O. N. Mesquita, S. Kane, and J. P. Gollub, *Phys. Rev. A* **45**, 3700 (1992).
- [25] E. Knobloch and J. B. Weiss, *Phys. Rev. A* **36**, 1522 (1987).
- [26] E. Moses and V. Steinberg, *Phys. Rev. Lett.* **60**, 2030 (1988).
- [27] T. Bohr and J. L. Hansen, *Chaos* **6**, 554 (1996).
- [28] S. M. Cox, P. G. Drazin, S. C. Ryrie, and K. Slater, *J. Fluid Mech.* **214**, 517 (1990).
- [29] S. Wiggins, *Chaotic Transport in Dynamical Systems* (Springer-Verlag, New York, 1992).
- [30] S. C. Ryrie, *J. Fluid Mech.* **236**, 1 (1992).
- [31] V. Rom-Kedar, A. Leonard, and S. Wiggins, *J. Fluid Mech.* **214**, 347 (1990).
- [32] T. H. Solomon and J. P. Golub, *Phys. Fluids* **31**, 1372 (1988).